Physica A 605 (2022) 128057

Contents lists available at ScienceDirect

Physica A

journal homepage: www.elsevier.com/locate/physa

Signatures of topological phase transitions in higher Landau levels of HgTe/CdTe quantum wells from an information theory perspective

Manuel Calixto [a,b,*], Nicolás A. Cordero [b,c], Elvira Romera [b,d], Octavio Castaños [e]

[a] Departamento de Matemática Aplicada, Universidad de Granada, Fuentenueva s/n, 18071 Granada, Spain
[b] Instituto Carlos I de Física Teórica y Computacional, Universidad de Granada, Fuentenueva s/n, 18071 Granada, Spain
[c] Departamento de Física and International Center for Critical Raw Materials (ICCRAM), Universidad de Burgos, Burgos, Spain
[d] Departamento de Física Atómica, Molecular y Nuclear, Universidad de Granada, Fuentenueva s/n, 18071 Granada, Spain
[e] Instituto de Ciencias Nucleares, Universidad Nacional Autónoma de México, Apdo. Postal 70-543, 04510, CDMX, Mexico

ARTICLE INFO

Article history:
Received 2 July 2022
Received in revised form 8 August 2022
Available online 13 August 2022

Keywords:
Topological phases
2D Dirac materials
Landau levels
Information theory

ABSTRACT

We analyze the structure of low energy Hamiltonian eigenstates in zincblende heterostructures (like HgTe/CdTe quantum wells) near the gamma point, under magnetic fields, to characterize topological phase transitions (TPT) under an information-theoretic perspective. Using information markers like entanglement, quantum fluctuations, fidelity susceptibility, participation ration, area in phase space, etc., we realize that higher Landau levels (LL) feel the topological phase transition slightly displaced with regard to the edge state, thus leading to the concept of "higher Landau level $|n| > 0$ TPT", as "echoes" of the standard edge state $n = 0$ TPT. We compute the critical magnetic field and the critical HgTe layer thickness at which these information measures of higher Landau levels undergo a structural change.

1. Introduction

Understanding quantum phases of matter and harnessing them for quantum technological applications (electronics, catalysis, quantum computing, etc.) is a topic of great importance today, specially those phases of a topological nature. For example, low-dimensional quantum devices based on mercury telluride–cadmium telluride (HgTe/CdTe) quantum wells (QWs) have been recently proposed in [1]. High-temperature superconductors and two-dimensional Dirac materials provide new types of topological phases, sometimes characterized by exotic electronic (edge) states and currents remarkably robust to impurities and thermal fluctuations. Quantum Hall effect provides the paradigmatic example of a topological phase, but dispersionless edge currents also appear in the absence of a magnetic field, for example, in some graphene analogues (silicene, germanene, etc. [2]) with a strong spin–orbit coupling [3–6]. Two-dimensional topological insulators (see [7–9] for text books, [10,11] for reviews and [12] for progress and prospects) were predicted theoretically by Kane and Mele [13] using a two-dimensional graphene-like material model with spin–orbit interaction. They were first proposed [14] and later-on observed experimentally [15] in HgTe/CdTe QWs.

Topological phases are founded on much different principles than Landau's theory, and they turn out to be characterized by topological numbers like: Chern, Pontryagin, Skyrmion, etc. and other kinds of winding numbers. Here we want to

* Corresponding author at: Departamento de Matemática Aplicada, Universidad de Granada, Fuentenueva s/n, 18071 Granada, Spain.
E-mail addresses: calixto@ugr.es (M. Calixto), ncordero@ubu.es (N.A. Cordero), eromera@ugr.es (E. Romera), ocasta@nucleares.unam.mx (O. Castaños).

https://doi.org/10.1016/j.physa.2022.128057

Table 1
Material parameters for HgTe/CdTe quantum wells with different HgTe layer thicknesses λ [11].

λ (nm)	α (meV nm)	β (meV nm^2)	δ (meV nm^2)	μ (meV)
5.5	387	−480	−306	9
6.1	378	−553	−378	−0.15
7.0	365	−686	−512	−10

contribute to the identification and to the reformulation of topological order through quantum information measures and concepts. While information theory has played an important role in the understanding of quantum phase transitions from the perspective of symmetry-breaking (Landau theory) [16–20], it does not seem to have had the same relevance in the study of topological phases, except for important studies related with entanglement entropy (see e.g., [21,22]). Actually, entanglement is at the heart of the interplay between quantum information and quantum phases of matter, playing a fundamental role in the understanding of quantum phase transitions. Therefore, the formulation of the basic notion of phase and phase transition in terms of quantum information allows for a unified study of both symmetry-breaking (Landau) and topological order in a common general framework.

In this paper we shall explore topological phases of HgTe/CdTe QWs by using different information measures like: fidelity-susceptibility, expectation values of operators and their variances (quantum fluctuations), entanglement (linear, Wehrl, Rényi) entropies, and localization measures (inverse participation ratio, area) in configuration and phase spaces. This approach has been fruitful for the study of the band insulator to topological insulator transition in silicene [23–27] and phosphorene [28,29]. Here we will analyze the structure not only of the edge states, but also of the higher Landau levels (LL) of HgTe quantum wells, leading to an interesting concept of "higher Landau level topological phase transition" (HTPT for short), to be distinguished from the standard concept of "topological phase transition" (TPT) linked to a band inversion of edge (zero Landau level) states. Information measures of Landau levels will be represented sometimes as a function of the applied magnetic field B and sometimes as a function of the HgTe QW thickness λ, to find a significant structural change around the critical point B_c and λ_c of the TPT or the HTPT.

The organization of the paper is the following. In Section 2 we review the Hamiltonian model of a HgTe QW, we compute its eigenspectrum and we discuss the topological phases of the system; we also introduce the concept of "higher Landau level topological phase transition" (HTPT), which involves a valence-conduction role inversion, which will be useful in the rest of the paper. In Section 3 we discuss several information-theoretic concepts linked to Hamiltonian eigenstates, which turn out to provide good markers of the TPT and the HTPT, displaying characteristic values around the TPT critical point. We plot (entanglement) purity, operator values and their variances, fidelity-susceptibility, inverse participation ratio and area in phase space of Landau levels as a function of the magnetic field B and the HgTe layer thickness λ. These are information-theoretic markers of the HTPT that indicate a sudden change in the structure of the Landau levels across the critical point. Finally, Section 4 is left for conclusions and outlook.

2. Hamiltonian model and topological phases

In [14,15,30–32] it was shown that quantum spin Hall effect can be realized in mercury telluride–cadmium telluride semiconductor quantum wells. The surface states in these 3D topological insulators can be described by a 2D modified effective Dirac Hamiltonian

$$H = \begin{pmatrix} H_+ & 0 \\ 0 & H_- \end{pmatrix}, \; H_s(\boldsymbol{k}) = \epsilon_0(\boldsymbol{k})\tau_0 + \boldsymbol{d}_s(\boldsymbol{k})\cdot\boldsymbol{\tau}, \tag{1}$$

where $s = \pm 1$ is the spin, $\boldsymbol{\tau} = (\tau_x, \tau_y, \tau_z)$ is the Pauli matrix vector (τ_0 denotes the 2×2 identity matrix) and $\boldsymbol{k} = (k_x, k_y)$ denotes the two-dimensional wavevector in the first Brillouin zone (FBZ). The spin up H_+ and down H_- Hamiltonians are conjugated and temporarily reversed, i.e. $H_-(\boldsymbol{k}) = H_+^*(-\boldsymbol{k})$. The expansion of the two-band Hamiltonian $H_s(\boldsymbol{k})$ about the center Γ of the FBZ gives

$$\epsilon_0(\boldsymbol{k}) = \gamma - \delta\boldsymbol{k}^2, \quad \boldsymbol{d}_s(\boldsymbol{k}) = (\alpha s k_x, \alpha k_y, \mu - \beta\boldsymbol{k}^2), \tag{2}$$

where $\alpha, \beta, \gamma, \delta$ and μ are expansion parameters that depend on the heterostructure (the HgTe layer thickness λ). The most important one is the mass or gap parameter μ, which changes sign at the critical HgTe layer thickness $\lambda_c \approx 6.3$ nm when going from the normal ($\lambda < \lambda_c$ or $\mu/\beta < 0$) to the inverted ($\lambda > \lambda_c$ or $\mu/\beta > 0$) regime. The term $\beta\boldsymbol{k}^2$ is also identified in [33] with the typical Wilson term $\ell W\boldsymbol{k}^2/2$ introduced to avoid the Fermion doubling problem arising when putting the continuous 2D Dirac equation into a lattice model (ℓ is the lattice constant); the gap μ is related to the magnetic moment.

Typical values of these parameters for different HgTe layer thickness (below and above λ_c) can be found in [11] and in Table 1 (γ can be neglected).

The energy of the two (conduction and valence) bands is

$$\epsilon_\pm(\boldsymbol{k}) = \epsilon_0(\boldsymbol{k}) \pm \sqrt{\alpha^2\boldsymbol{k}^2 + (\mu - \beta\boldsymbol{k}^2)^2}. \tag{3}$$

To distinguish between topological phases, it is customary to use the Chern–Pontryagin topological number (related to the quantum spin Hall conductance), which can be calculated by the TKNN (Thouless–Kohmoto–Nightingale–Nijs) formula

$$\mathcal{C} = \frac{1}{2\pi}\iint_{\mathrm{FBZ}} d^2\boldsymbol{k}\left(\frac{\partial\hat{\boldsymbol{d}}(\boldsymbol{k})}{\partial k_x}\times\frac{\partial\hat{\boldsymbol{d}}(\boldsymbol{k})}{\partial k_y}\right)\cdot\hat{\boldsymbol{d}}(\boldsymbol{k}), \tag{4}$$

with $\hat{\boldsymbol{d}} = \boldsymbol{d}/|\boldsymbol{d}|$ the unit vector in the direction of $\boldsymbol{d}$. The Chern–Pontryagin number counts the number of times (winding number) the unit vector $\hat{\boldsymbol{d}}(\boldsymbol{k})$ wraps around the unit sphere as $\boldsymbol{k}$ wraps around the entire FBZ. Topological phases also emerge in open quantum systems with engineered dissipation [34–36]. One approach that has gained attraction lately is the use of effective non-Hermitian Hamiltonians [37–40] and their associated Chern numbers [41]. Other generalized Chern numbers based on open system Green's functions have been recently proposed in [42]. In this article, we shall restrict ourselves to the standard closed quantum system case.

The TKNN formula (4) for $\boldsymbol{d}_s(\boldsymbol{k})$ in (2) provides the Chern number

$$\mathcal{C}_s = s[\mathrm{sign}(\mu) + \mathrm{sign}(\beta)], \tag{5}$$

where we have integrated on the whole plane, as corresponds to the continuum limit $\ell \to 0$ (zero lattice constant). One can also work with a lattice regularization (tight-binding) of the continuum model just replacing $k_{x,y} \to \ell^{-1}\sin(k_{x,y}\ell)$ and $k_{x,y}^2 \to 2\ell^{-2}(1-\cos(k_{x,y}\ell))$. When $\mathrm{sign}(\beta)$ does not change (see e.g. typical values in Table 1), it is $\mathrm{sign}(\mu)$ which determines the topological phase. Sometimes, it is also discussed in terms of $\mathrm{sign}(\mu/\beta)$, as done before.

A similar calculation for other 2D-Dirac materials of group IV (graphene analogues, but with an intrinsic non-zero spin–orbit coupling Δ_{so}, like silicene, germanene, stanene, etc.) with $\boldsymbol{d}_{s\xi} = (v\hbar\xi k_x, v\hbar k_y, \Delta_{s\xi})$ ($\xi = \pm 1$ denotes the valley index and v the Fermi velocity) gives the Chern number $\mathcal{C}_{s\xi} = \xi\,\mathrm{sign}(\Delta_{s\xi})$, with $\Delta_{s\xi} = (\Delta_z - s\xi\Delta_{\mathrm{so}})/2$ the Dirac mass, which can be tunned by an external electric field potential Δ_z [43–46].

We shall propose alternative topological phase transition markers based on information-theoretic measures of Landau levels. For it, we shall firstly introduce a magnetic field interaction.

Promoting the wave-vector $\boldsymbol{k}$ to the momentum operator $\boldsymbol{k} \to \boldsymbol{p}/\hbar = -\mathrm{i}\nabla$, the interaction with a perpendicular magnetic field $\boldsymbol{B} = (0,0,B)$ is introduced through the usual minimal coupling, $\boldsymbol{p} \to \boldsymbol{P} = \boldsymbol{p} + e\boldsymbol{A}$ with $\boldsymbol{A} = (A_x, A_y) = (-By, 0)$ and e the elementary charge (in absolute value). The general prescription for magnetic field coupling is then to substitute

$$k_x \to P_x/\hbar = \frac{a^\dagger + a}{\sqrt{2}\ell_B}, \quad k_y \to P_y/\hbar = \frac{a^\dagger - a}{\mathrm{i}\sqrt{2}\ell_B}. \tag{6}$$

in terms of creation $a^\dagger$ and annihilation

$$a = \frac{\ell_B}{\sqrt{2}\hbar}(P_x - \mathrm{i}P_y) = \frac{-1}{\sqrt{2}\ell_B}(y - y_0 + \mathrm{i}\ell_B^2 p_y/\hbar), \tag{7}$$

operators, where $\ell_B = \sqrt{\hbar/(eB)}$ is the magnetic length and $y_0 = \ell_B^2 k_x$ is the (conserved) center coordinate of the cyclotron orbit. After Peierls' substitution, the Hamiltonian (1),(2) can be written as

$$H_+ = \begin{pmatrix} \gamma+\mu-\frac{(\delta+\beta)(2N+1)}{\ell_B^2} & \frac{\sqrt{2}\alpha}{\ell_B}a \\ \frac{\sqrt{2}\alpha}{\ell_B}a^\dagger & \gamma-\mu-\frac{(\delta-\beta)(2N+1)}{\ell_B^2} \end{pmatrix},$$
$$H_- = \begin{pmatrix} \gamma+\mu-\frac{(\delta+\beta)(2N+1)}{\ell_B^2} & -\frac{\sqrt{2}\alpha}{\ell_B}a^\dagger \\ -\frac{\sqrt{2}\alpha}{\ell_B}a & \gamma-\mu-\frac{(\delta-\beta)(2N+1)}{\ell_B^2} \end{pmatrix}, \tag{8}$$

where $N = a^\dagger a$ is the Landau level number operator. Note that the operator $M_s = N + s/2(\tau_z + s)$ is a conserved quantity (commutes with the Hamiltonian H_s) and therefore can be used to label the Hamiltonian eigenvectors of the system. A Zeeman term contribution

$$H_s^Z = -\frac{s}{2}B\mu_{\mathrm{B}}\left(g_{\mathrm{e}}\frac{\tau_0+\tau_z}{2} + g_{\mathrm{h}}\frac{\tau_0-\tau_z}{2}\right) \tag{9}$$

can also be added to the Hamiltonian, with $\mu_{\mathrm{B}} \simeq 0.058$ meV/T the Bohr magneton and $g_{\mathrm{e,h}}$ the effective (out-of-plane) g-factors for electrons and holes (conduction and valence bands).

Using (Fock state) eigenvectors $||n|\rangle$ of the Landau level number operator $N = a^\dagger a$, one can analytically obtain the eigenspectrum

$$E_n^s = \gamma - \frac{2\delta|n| - s\beta}{\ell_B^2} - s\frac{g_{\mathrm{e}}+g_{\mathrm{h}}}{4}B\mu_{\mathrm{B}} + \mathrm{sgn}(n)\sqrt{\frac{2\alpha^2|n|}{\ell_B^2} + \left(\mu - \frac{2\beta|n| - s\delta}{\ell_B^2} - s\frac{g_{\mathrm{e}}-g_{\mathrm{h}}}{4}B\mu_{\mathrm{B}}\right)^2}, \tag{10}$$

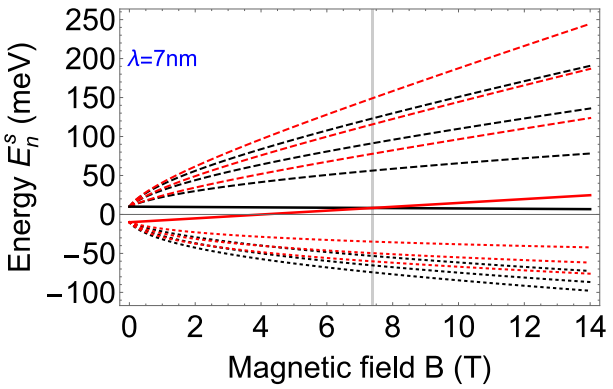

Fig. 1. Low-energy spectra E_n^s of a HgTe/CdTe quantum well as a function of the magnetic field B for HgTe layer thickness $\lambda = 7$ nm. Landau levels $n = \pm 1, \pm 2, \pm 3$ are represented by dotted (holes) and dashed (electrons) thin lines, black for spin $s = 1$ and red for $s = -1$. Edge states ($n = 0$) are represented by thick lines. The vertical gray grid line indicates the critical magnetic field $B_c \simeq 7.4$ T separating QSH from QH regimes.

for Landau level index $n = \pm 1, \pm 2, \pm 3, \ldots$ [valence $(-)$ and conduction $(+)$], and

$$E_0^s = \gamma - s\mu - \frac{\delta - s\beta}{\ell_B^2} - B\mu_B\left(\frac{s+1}{4}g_h + \frac{s-1}{4}g_e\right), \tag{11}$$

for the $n = 0$ edge states. These eigenvalues coincide with those of [47–49] for the identification $s = \{-1, 1\} = \{\uparrow, \downarrow\}$. The corresponding Hamiltonian eigenvectors are

$$|\boldsymbol{n}\rangle_s = \begin{pmatrix} A_n^s \left||n| - \frac{s+1}{2}\right\rangle \\ \\ B_n^s \left||n| + \frac{s-1}{2}\right\rangle \end{pmatrix}, \tag{12}$$

with coefficients

$$\begin{aligned} A_n^s &= \begin{cases} \frac{\mathrm{sgn}(n)}{\sqrt{2}}\sqrt{1 + \mathrm{sgn}(n)\cos\vartheta_n^s}, & n \neq 0, \\ (1-s)/2, & n = 0, \end{cases} \\ B_n^s &= \begin{cases} \frac{s}{\sqrt{2}}\sqrt{1 - \mathrm{sgn}(n)\cos\vartheta_n^s}, & n \neq 0, \\ (1+s)/2, & n = 0, \end{cases} \end{aligned} \tag{13}$$

where

$$\vartheta_n^s = \arctan\left(\frac{\sqrt{2|n|}\,\alpha/\ell_B}{\mu - \frac{2\beta|n| - s\delta}{\ell_B^2} - s\frac{g_e - g_h}{4}B\mu_B}\right). \tag{14}$$

The coefficients A_n^s and B_n^s can eventually be written as sine and cosine of half angle ϑ_n^s, depending on $\mathrm{sgn}(n)$. Later in Fig. 2 (top left panel) we represent the angle ϑ_n^s as a function of the magnetic field B, and in Fig. 3 (top right panel) as a function of the HgTe layer thickness λ, ranging from zero to π, with a value of $\vartheta_n^s \simeq \pi/2$ around the TPT critical point, in both cases. In fact, we shall see that ϑ_n^s plays a role in the identification of the HTPT.

The two zero Landau levels E_0^+ and E_0^- belong to different (conduction and valence) bands. The level crossing condition

$$E_0^+ = E_0^- \Rightarrow B_c = \frac{\mu}{e\beta/\hbar - \mu_B(g_e + g_h)/4}, \tag{15}$$

gives the critical magnetic field B_c which separates the Quantum Spin Hall (QSH) from the Quantum Hall (QH) regime [48]. For example, for the material parameters in Table 1 corresponding to a QW thickness $\lambda = 7.0$ nm and $g_e = 22.7, g_h = -1.21$, one obtains $B_c \simeq 7.4$ T. Therefore, for magnetic fields $B > B_c$, the model shows an inverted band structure (see Fig. 1 for the low-energy spectrum E_n^s as a function of the magnetic field B, and later in Fig. 3 as a function of the HgTe layer thickness λ).

Higher Landau levels $|n| > 0$ feel the TPT at a different place than edge states $n = 0$. In fact, we shall see that higher Landau levels undergo a structural change when the angle (14) takes the value $\vartheta_n^s = \pi/2$ (which means $|A_n^s| = |B_n^s|$), that is, when

$$\mu - \frac{2\beta|n| - s\delta}{\ell_B^2} - s\frac{g_e - g_h}{4}B\mu_B = 0. \tag{16}$$

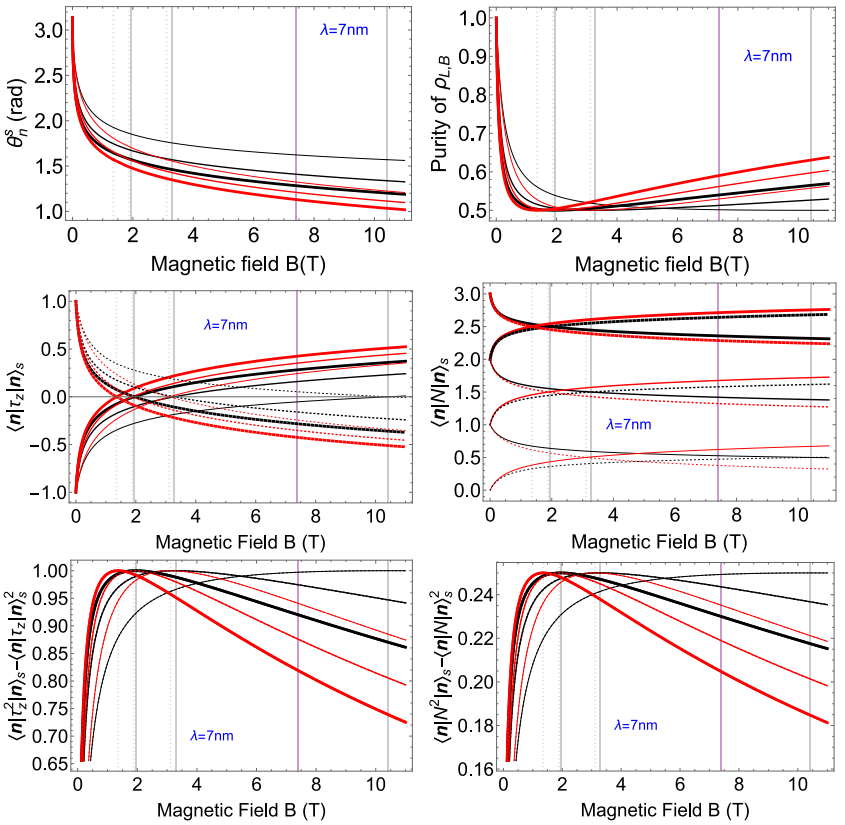

Fig. 2. Angle ϑ_n^s (14), purity (19) and expectation values (20) and variances of N and τ_z, for the Hamiltonian eigenvectors $|\boldsymbol{n}(\lambda)\rangle_s$, $n=\pm1,\pm2,\pm3$ (line thickness grows with $|n|$), as a function of the magnetic field B for a HgTe layer thickness of $\lambda=7$ nm. Electron (resp. hole) states $n>0$ (resp. $n<0$) are represented by solid (resp. dotted) lines, black for spin $s=1$ and red for $s=-1$. The vertical purple grid line indicates the critical magnetic field $B_c=7.4$ T separating normal (QH) from inverted (QSH) regimes. Vertical gray grid lines mark the critical magnetic fields $B_c^{n,s}$ (17) of the HTPT.

This condition provides a new spin-dependent critical magnetic field

$$B_c^{n,s}=\frac{\mu}{e(2\beta|n|-s\delta)/\hbar+s\mu_{\rm B}(g_{\rm e}-g_{\rm h})/4}, \tag{17}$$

which deviates from (15) for higher Landau levels $|n|>0$ (see later in Fig. 4). We shall refer to this phenomenon as a "higher Landau level TPT" (HTPT), to distinguish it from the standard edge state ($n=0$) TPT. Note that, at $\vartheta_n^s=\pi/2$, the spinor coefficients (13) of a Hamiltonian eigenvector (12) have the same weight, that is $|A_n^s|=|B_n^s|$. Therefore, at $\vartheta_n^s=\pi/2$, valence and conduction contributions interchange their roles. This is a kind of "band inversion" for higher Landau levels that justifies the term HTPT.

3. Information-theoretic markers of the topological phase transition

3.1. Reduced density matrix and purity

Before calculating some operator expectation values and their variances, let us make explicit the reduced density matrices associated to a Hamiltonian eigenstate $\rho^{n,s}=|\boldsymbol{n}\rangle_s\langle\boldsymbol{n}|$ for a composite system given by Landau (L) and Band (B) sectors, that is

$$\begin{aligned}\rho_L^{n,s}&={\rm tr}_B(\rho^{n,s})=(A_n^s)^2\left||n|-\frac{s+1}{2}\right\rangle\left\langle|n|-\frac{s+1}{2}\right|+(B_n^s)^2\left||n|+\frac{s-1}{2}\right\rangle\left\langle|n|+\frac{s-1}{2}\right|,\\ \rho_B^{n,s}&={\rm tr}_L(\rho^{n,s})=\begin{pmatrix}(A_n^s)^2&0\\0&(B_n^s)^2\end{pmatrix}.\end{aligned} \tag{18}$$

The purity of a Hamiltonian eigenstate in both cases is

$$P_n^s={\rm tr}(\rho_{L,B}^{n,s})^2=(A_n^s)^4+(B_n^s)^4. \tag{19}$$

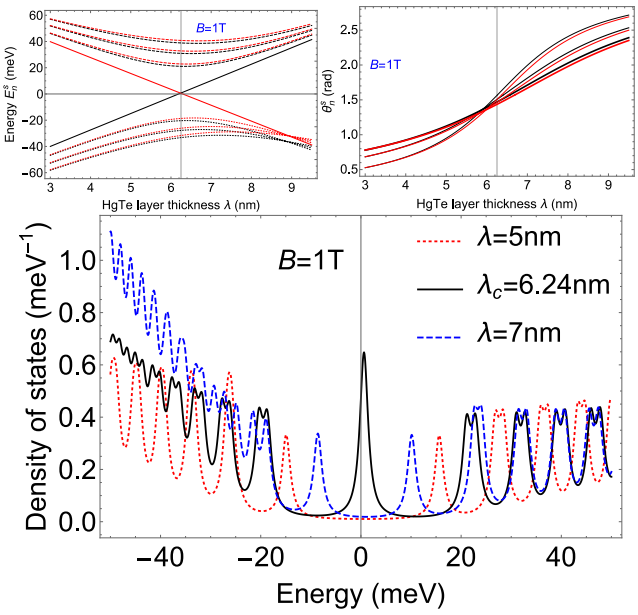

Fig. 3. Top panel: Low-energy spectra E_n^s and angle ϑ_n^s of a HgTe/CdTe quantum well as a function of the HgTe layer thickness λ for $B = 1$ T $\Rightarrow \lambda_c(B) \simeq 6.24$ nm. Landau levels $n = \pm 1, \pm 2, \pm 3$ are represented by dotted (holes) and dashed (electrons) thin lines, black for spin $s = 1$ and red for $s = -1$. Edge states ($n = 0$) are represented by thick lines. Vertical gray grid lines indicate the critical HgTe thickness $\lambda_c(B)$ separating normal (QH) from inverted (QSH) regimes. Bottom panel: Density of states (we choose $\eta = 1$) as a function of the energy for $B = 1$ T and three different values of the HgTe layer thickness below and above the critical value $\lambda_c(B) = 6.24$ nm.

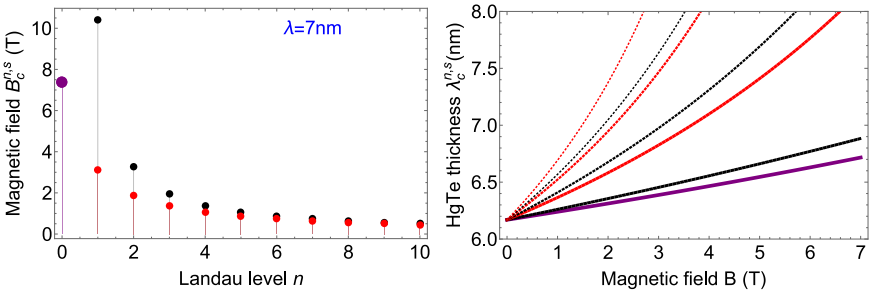

Fig. 4. Left panel: Critical magnetic field $B_c^{n,s}$ in Eq. (17) of the HTPT as a function of the Landau level n for HgTe layer thickness $\lambda = 7$ nm (black dots for spin $s = 1$ and red dots for $s = -1$). The thick purple dot ($n = 0$) corresponds to the critical B_c of the ordinary TPT in Eq. (15). Right panel: Critical HgTe thickness $\lambda_c^{n,s}$ (22),(24) as a function of the applied magnetic field B for the edge ($n = 0$) state (thick purple line) and the Landau levels $n = 1$ (solid), $n = 2$ (dashed) and $n = 3$ (dotted), in decreasing thickness (black for spin $s = 1$ and red for $s = -1$).

Purity P is related to linear entropy L by $L_n^s = 1 - P_n^s$. In Fig. 2 (top right panel) we plot the purity of low-energy Hamiltonian eigenstates as a function of the magnetic field, which reveals a sudden increase of entanglement (a decrease in purity) between L and B sectors at the HTPT critical point $B_c^{n,s}$ in Eq. (17). This entanglement is the same for electrons and holes $P_n^s = P_{-n}^s$, with a small dependence on spin. The growth of entanglement around the HTPT is most apparent when we represent purity as a function of the HgTe layer thickness λ (see later in Fig. 5, bottom right panel), where $P_n^s(\lambda)$ displays a minimum around the critical thickness $\lambda_c^{n,s}(B)$ [see later in Eq. (22)] for a given magnetic field B. These minima are displaced with respect to the TPT critical thickness λ_c for larger and larger $|n|$. This will be a common feature of most of the HTPT markers proposed here, which show that higher-energy Hamiltonian eigenstates feel the topological phase transition displaced with respect to lower-energy Hamiltonian eigenstates. This is a shared feature with the so called "Excited State Quantum Phase Transitions" (ESQPT) already present in the literature [50,51]. ESQPT is a continuation of the concept of QPT for singularities of the ground state to singularities of the excites states and singular level densities.

Therefore, entanglement turns out to be a good marker of the TPT in HgTe QWS at low magnetic fields, and of the HTPT in general.

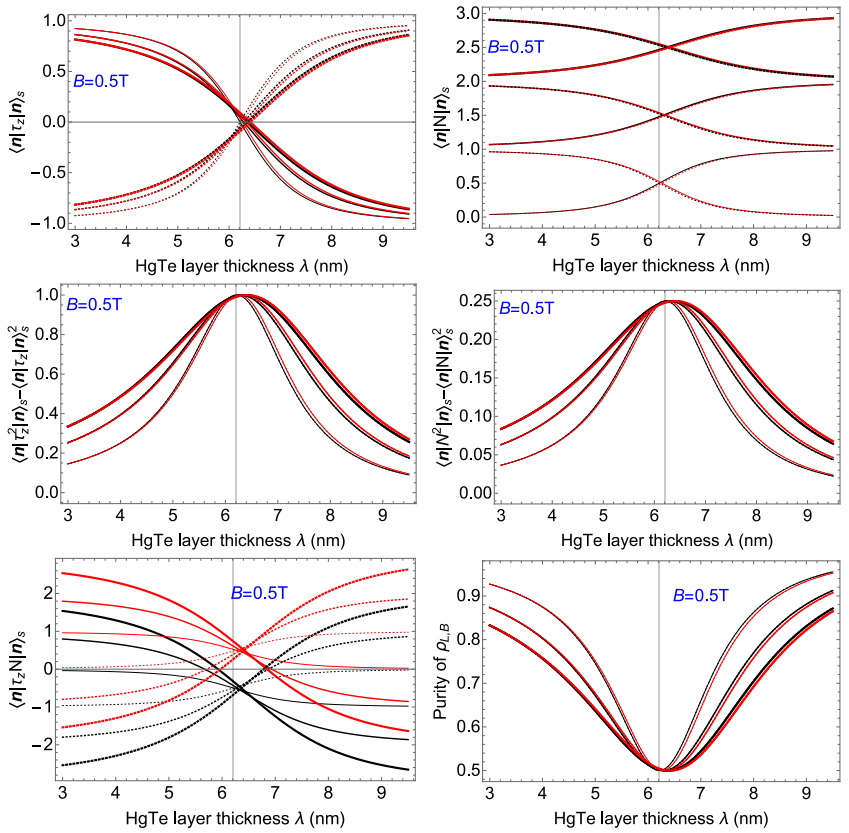

Fig. 5. Purity, average values $\langle \boldsymbol{n}|\tau_z|\boldsymbol{n}\rangle_s$, $\langle \boldsymbol{n}|N|\boldsymbol{n}\rangle_s$ and $\langle \boldsymbol{n}|\tau_z N|\boldsymbol{n}\rangle_s$ and their variances for electrons $n > 0$ (solid lines) and holes $n < 0$ (dotted lines) of Hamiltonian eigenvectors $|\boldsymbol{n}(\lambda)\rangle_s$ for a HgTe/CdTe quantum well as a function of the HgTe layer thickness λ for Landau levels $n = \pm 1, \pm 2, \pm 3$ (line thickness grows with $|n|$) and magnetic field $B = 0.5$ T. Black lines for spin $s = 1$ and red lines for $s = -1$. Vertical gray grid lines indicate the critical HgTe thickness $\lambda_c(B)$ separating normal (QH) from inverted (QSH) regimes.

3.2. Operator averages and their variances

Looking for other signatures of the HTPT, in Fig. 2 we represent the expectation values of the Pauli (valence/conduction band) matrix and the Landau level number $N = a^\dagger a$

$$\begin{aligned}\langle \boldsymbol{n}|\tau_z|\boldsymbol{n}\rangle_s &= \mathrm{tr}(\tau_z \rho_B^{n,s}) = (A_n^s)^2 - (B_n^s)^2,\\ \langle \boldsymbol{n}|N|\boldsymbol{n}\rangle_s &= \mathrm{tr}(N \rho_L^{n,s}) = (A_n^s)^2 \left(|n| - \frac{s+1}{2}\right) + (B_n^s)^2 \left(|n| + \frac{s-1}{2}\right),\end{aligned} \tag{20}$$

and their variances for low-energy Hamiltonian eigenvectors $|\boldsymbol{n}\rangle_s$.

We perceive a kind of inversion behavior of these mean values occurring at the critical values $B_c^{n,s}$ in (17). We also perceive a growth of fluctuations (greater variance) for these average values around the HTPT region. We shall see later in Fig. 5 that these HTPT markers turn out to be sharper when considered as a function of the HgTe layer thickness λ instead of B.

From now on we shall discard Zeeman coupling for the sake of simplicity and convenience. Although discarding Zeeman coupling modifies the values of B_c in (15) (namely from $B_c \simeq 7.4\ T$ to $B_c \simeq 9.6\ T$ for $\lambda = 7$ nm) and of $B_c^{n,s}$ in (17), our main conclusions about quantum information signatures of the HTPT remain qualitatively equivalent. We shall then use a linear fit

$$\begin{aligned}\mu(\lambda) &= 77.31 - 12.53\lambda,\\ \alpha(\lambda) &= 467.49 - 14.65\lambda,\\ \beta(\lambda) &= 283.58 - 138.16\lambda,\\ \delta(\lambda) &= 458.46 - 138.25\lambda,\end{aligned} \tag{21}$$

Table 2
Critical HTPT HgTe layer thickness $\lambda_c^{n,s}(B)$ in (24) (in nanometers) for two values of the magnetic field, $B = 0.5$ T and $B = 1$ T, as a function of the Landau level $n = 1, 2, 3$ and the spin $s = \pm 1$. To be compared with the critical TPT ($n = 0$) HgTe layer thickness $\lambda_c(0.5) = 6.2$ nm and $\lambda_c(1) = 6.24$ nm.

$\lambda_c^{n,s}(0.5)$	$n = 1$	$n = 2$	$n = 3$
$s = 1$	6.21	6.29	6.36
$s = -1$	6.26	6.34	6.41
$\lambda_c^{n,s}(1)$	$n = 1$	$n = 2$	$n = 3$
$s = 1$	6.26	6.41	6.57
$s = -1$	6.36	6.52	6.69

of the material parameters in Table 1 as a function of the HgTe thickness λ. In all cases the coefficient of determination is $R^2 > 0.99$. Inserting these values of $\alpha, \beta, \mu, \delta$ in (15), this linear fit gives us a relation

$$\lambda_c(B) = \frac{368.31 - 2.05B}{59.7 - B} \tag{22}$$

between the applied magnetic field B and the critical thickness $\lambda_c(B)$ at which the TPT (band inversion $E_0^+ = E_0^-$) takes place. For example, the zero field critical thickness yields $\lambda_c(0) \simeq 6.17$ nm, whereas $\lambda_c(1) \simeq 6.24$ nm, as can be seen in Fig. 3, top left panel, where we represent the Hamiltonian eigenspectrum as a function of the HgTe layer thickness λ. In this Figure (bottom panel) we also represent the low-energy density of states

$$D_\eta(\varepsilon) = \sum_{s=\pm 1} \sum_{n=-\infty}^{\infty} \delta_\eta(\varepsilon - E_n^s), \tag{23}$$

as a function of the energy ε for $B = 1$ T and three different values of the HgTe layer thickness: below ($\lambda = 5$ nm) and above ($\lambda = 7$ nm) the critical value $\lambda_c(B) = 6.24$ nm. Here we are using the Lorentzian $\delta_\eta(x) = (\eta/\pi)/(\eta^2 + x^2) \to \delta(x)$ as a finite representation/regularization of the Dirac delta for small η. The critical case $\lambda_c(B) = 6.24$ nm is distinguished by a sudden growth of $D_\eta(\varepsilon)$ around $\varepsilon = 0$ due to edge states.

For higher Landau levels $n > 0$, the critical HgTe thickness obtained from condition (17) gives

$$\lambda_c^{n,s}(B) = \frac{77.31 - 0.86B|n| + 0.7Bs}{12.53 - 0.42B|n| + 0.21Bs}, \; n \neq 0. \tag{24}$$

In Fig. 4, right panel, we represent the critical HgTe thickness $\lambda_c(B)$ and $\lambda_c^{n,s}(B)$ for the TPT and the HTPT, respectively, as a function of B, for $n = 0, 1, 2, 3$. For low magnetic fields $B \ll 1$ T, all $\lambda_c^{n,s}$ converge to λ_c but, for large B, they differ significantly. In the following plots, we shall mostly take $B = 0.5$ T, so that the HTPT critical points $\lambda_c^{n,s}(0.5)$ slightly differ from $\lambda_c(0.5) = 6.2$ nm, for low energy Hamiltonian eigenvectors ($|n| = 1, 2, 3$). In Table 2 we provide particular values of $\lambda_c^{n,s}(B)$ for two magnetic fields, $B = 0.5$ T and $B = 1$ T, and several Hamiltonian eigenstates. This corresponds to two different cross sections of the plot 4 (right panel) at $B = 0.5$ T and $B = 1$ T, respectively. This behavior can also be perceived in Fig. 3, top right panel, where we represent the angle θ_n^s as a function of the HgTe layer thickness λ for $B = 1$ T, and where the band inversion $\theta_n^s = \pi/2$ occurs near $\lambda_c(1) = 6.24$ nm.

As we did in Fig. 2, in Fig. 5 we plot again the average values of τ_z and N, and their fluctuations, but this time as a function of the HgTe layer thickness λ. Together with purity (19), fluctuations turn out to be sharp markers of the HTPT, displaying conspicuous maxima and minima at the HTPT critical points $\lambda_c^{n,s}(B)$ which, as we have already emphasized, appear slightly displaced to the right with respect to the TPT critical point $\lambda_c(B)$.

3.3. Fidelity susceptibility

The fidelity is an elemental concept in general information theory, measuring the accuracy of a transmission. In quantum theory, the fidelity between two normalized pure states $|\psi_1\rangle$ and $|\psi_2\rangle$ is just given by the scalar product $F = |\langle\psi_1|\psi_2\rangle|^2$, that is, the squared cosine of the angle between the two vectors. Therefore, it is a measure of the closeness between $|\psi_1\rangle$ and $|\psi_2\rangle$, with $F = 1$ indicating that the states are the same up to a global phase and $F = 0$ when they are orthogonal. Since QPTs are characterized by a sudden change on the ground state structure around the critical value of some control parameter λ, fidelity turns out to be a good marker/precursor of the QPT even for finite size systems (see details in [16,52–56]). Therefore, we will study the fidelity between the quantum states at λ and $\lambda + \delta\lambda$:

$$F_\psi(\lambda, \lambda + \delta\lambda) = |\langle\psi(\lambda)|\psi(\lambda + \delta\lambda)\rangle|^2, \tag{25}$$

which will show a minimum ($dF_\psi/d\lambda|_{\lambda=\lambda_c} = 0$) at λ_c where the system changes drastically. Therefore, the most representative term of the Taylor series expansion of F_ψ for small $\delta\lambda$ is the second derivative or *fidelity susceptibility*

$$\chi_\psi(\lambda) = 2\frac{1 - F_\psi(\lambda, \lambda + \delta\lambda)}{\delta\lambda^2} \tag{26}$$

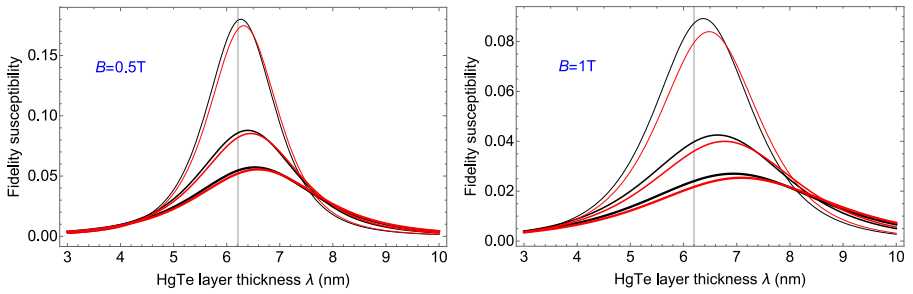

Fig. 6. Fidelity susceptibility (26) between the Hamiltonian eigenvectors $|\boldsymbol{n}(\lambda)\rangle_s$ and $|\boldsymbol{n}(\lambda+\delta\lambda)\rangle_s$ ($\delta\lambda = 0.001$) of a HgTe/CdTe quantum well for magnetic fields $B = 0.5$ T (left) and $B = 1$ T (right) as a function of the HgTe layer thickness λ for the first three conduction Landau levels $n = 1, 2, 3$ (same result for valence LL), black lines for spin $s = 1$ and red lines for $s = -1$. (Line thickness grows with $|n|$). Vertical gray grid lines indicate the critical HgTe thickness $\lambda_c(0.5) \simeq 6.2$ nm and $\lambda_c(1) \simeq 6.24$ nm separating normal (QH) from inverted (QSH) regimes.

which is less sensitive to the choice of $\delta\lambda$. We propose this measure as a HTPT marker. In fact, in Fig. 6 we show that the fidelity susceptibility between the Hamiltonian eigenvectors $|\boldsymbol{n}(\lambda)\rangle_s$ and $|\boldsymbol{n}(\lambda+\delta\lambda)\rangle_s$ (we choose $\delta\lambda = 0.001$) as a function of the HgTe layer thickness λ (the "control parameter" in this case) attains its maximum at the HTPT critical value $\lambda_c^{n,s}(B)$; These maxima are slightly displaced to the right of the TPT critical value $\lambda_c(B)$ nm, according to Table 2. We get the same result for conduction and valence states. The fact that the maximum of $\chi_{|\boldsymbol{n}(\lambda)\rangle_s}$, occurring at $\lambda_c^{n,s}$, is shifted to the right of λ_c and is less and less sharp for larger $|n|$, says that higher-energy Hamiltonian eigenstates (in absolute value) feel the HTPT "less intensely" and displaced with respect to lower-energy Hamiltonian eigenstates. This displacement is more and more evident for higher magnetic fields, as we already anticipated in Fig. 4, right panel. As already shown in Fig. 5, this was also a characteristic of fluctuations and entanglement of Hamiltonian eigenstates, that time measured by purity (19).

3.4. Inverse participation ratio in position representation

The inverse participation ratio (IPR) measures the spread of a state $|\psi\rangle$ over a basis $\{|i\rangle\}_{i=1}^N$. More precisely, if p_i is the probability of finding the (normalized) state $|\psi\rangle$ in $|i\rangle$, then the IPR is defined as the second moment $M_\psi^2 = \sum_i p_i^2$. If $|\psi\rangle$ only "participates" of a single state $|i_0\rangle$, then $p_{i_0} = 1$ and $M_\psi^2 = 1$ is maximum, whereas if $|\psi\rangle$ equally participates on all of them (equally distributed), $p_i = 1/N, \forall i$, then $M_\psi^2 = 1/N$ is minimum. Therefore, the IPR is a measure of the localization of $|\psi\rangle$ in the corresponding basis.

Let us chose the position representation $|y\rangle$ to write the Hamiltonian eigenstates (12). We know that Fock states $|n\rangle$ can be written in position representation as

$$\langle y|n\rangle = \frac{1}{\sqrt{2^n n!\sqrt{\pi}}} e^{-y^2/2} H_n(y)\,, \tag{27}$$

where H_n are the Hermite polynomials of degree $n \geq 0$. The number-state density in position space is $\varrho_n(y) = |\langle y|n\rangle|^2$, which is normalized according to $\int_{-\infty}^{\infty} \varrho_n(y)dy = 1$. The density for the Hamiltonian eigenvectors (12) in position representation is calculated through the corresponding reduced density matrix ρ_L (Landau sector) in (18) as

$$\rho_n^s(y) = \langle y|\rho_L|y\rangle = (A_n^s)^2 \varrho_{|n|-\frac{s+1}{2}}(y) + (B_n^s)^2 \varrho_{|n|+\frac{s-1}{2}}(y). \tag{28}$$

The IPR $M_{n,s}^2$ of the density matrix $\rho^{n,s} = |\boldsymbol{n}\rangle_s\langle\boldsymbol{n}|$ of a Hamiltonian eigenstate in position representation is then calculated as the second moment of the density distribution

$$M_{n,s}^2 \equiv \int_{-\infty}^{\infty} \rho_n^s(y)^2 dy. \tag{29}$$

As a previous step, we need the following integrals of Hermite density products:

$$\mathcal{M}_{n,m} \equiv \int_{-\infty}^{\infty} \varrho_n(y)\varrho_m(y)dy = \frac{1}{\sqrt{2\pi}} \begin{pmatrix} 1 & \frac{1}{2} & \frac{3}{8} & \frac{5}{16} & \cdots \\ \frac{1}{2} & \frac{3}{4} & \frac{7}{16} & \frac{11}{32} & \cdots \\ \frac{3}{8} & \frac{7}{16} & \frac{41}{64} & \frac{51}{128} & \cdots \\ \frac{5}{16} & \frac{11}{32} & \frac{51}{128} & \frac{147}{256} & \cdots \\ \vdots & \vdots & \vdots & \vdots & \ddots \end{pmatrix}, \tag{30}$$

for $n, m = 0, 1, 2, 3\ldots$. Therefore, we can simply write (29) as (we denote $\mathcal{M}_{n,n} = \mathcal{M}_n$)

$$M_{n,s}^2 = (A_n^s)^4 \mathcal{M}_{|n|-\frac{s+1}{2}} + (B_n^s)^4 \mathcal{M}_{|n|+\frac{s-1}{2}} + 2(A_n^s)^2(B_n^s)^2 \mathcal{M}_{|n|,|n|+1}. \tag{31}$$

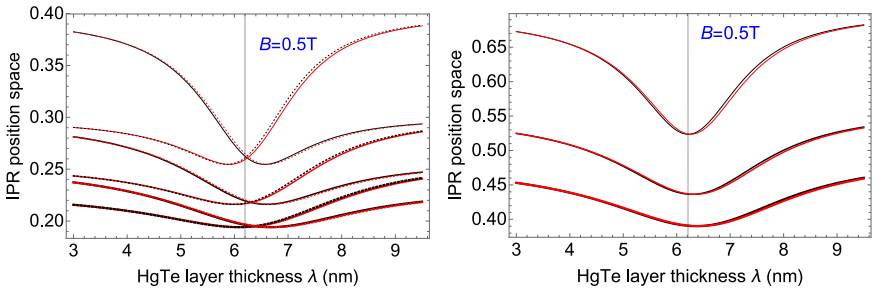

Fig. 7. Inverse participation ratio (31) for electrons $n > 0$ (solid lines) and holes $n < 0$ (dotted lines) of Hamiltonian eigenvectors of a HgTe/CdTe quantum well for a magnetic field of $B = 0.5$ T as a function of the HgTe layer thickness λ for Landau levels $n = \pm 1, \pm 2, \pm 3$ (line thickness grows with $|n|$), black lines for spin $s = 1$ and red lines for $s = -1$. Vertical gray grid lines indicate the critical HgTe thickness $\lambda_c(0.5) \simeq 6.2$ nm separating normal (QH) from inverted (QSH) regimes. The combined electron plus hole IPRs are shown in the right panel and exhibit minima at the corresponding HTPT critical point $\lambda_c^{n,s}(B)$.

In Fig. 7 (left panel) we represent the IPR of low-energy Hamiltonian eigenstates in position representation as a function of the HgTe layer thickness λ for a magnetic field of $B = 0.5$ T. Conduction and valence states display an inverted (mirror reflected) behavior at both sides of the HTPT point $\lambda_c^{n,s}(B)$ for a given spin s. We find that the combined (electron plus hole) IPR $M^2_{n,s}+M^2_{-n,s}$ exhibits a minimum near the HTPT critical point, as shown in the right panel of Fig. 7. This minimum is sharper for lower $|n|$. Therefore, we can conclude that lower $|n|$ Landau levels are more localized than higher $|n|$ LL, and the combination of electrons plus holes undergoes a sudden delocalization around the HTPT critical point, which is sharper for lower $|n|$.

3.5. Husimi function and area in phase space

Now we are going to analyze Hamiltonian eigenvectors in phase space, both in Landau (L) and band (B) sectors. For the Landau (Fock) sector, we have at our disposal an overcomplete set of harmonic oscillator (canonical or Glauber) coherent states $|\alpha\rangle$ which are obtained by displacing the Fock vacuum $|0\rangle$ as

$$|\alpha\rangle = e^{-|\alpha|^2/2} e^{\alpha a^\dagger} |0\rangle = e^{-|\alpha|^2/2} \sum_{n=0}^{\infty} \frac{\alpha^n}{\sqrt{n!}} |n\rangle, \tag{32}$$

with $\alpha = q + \mathrm{i}p \in \mathbb{C}$ a point in the phase space $\mathbb{C}$. "Position" q and "momentum" p are called quadratures in the argot of quantum optics. Coherent states verify the closure relation

$$1 = \int_{\mathbb{C}} |\alpha\rangle\langle\alpha| \frac{d^2\alpha}{\pi}, \tag{33}$$

with $d^2\alpha = dqdp$. For the band (B) sector, we have the typical SU(2) spin-1/2 (atomic, Bloch or Radcliffe [57]) coherent states

$$|\vartheta, \phi\rangle = \begin{pmatrix} \cos(\vartheta/2) \\ \sin(\vartheta/2) e^{\mathrm{i}\phi} \end{pmatrix}, \; d\Omega = \frac{1}{2\pi} \sin(\vartheta) d\vartheta d\phi \tag{34}$$

with integration measure $d\Omega$ (the solid angle on the Bloch sphere $\mathbb{S}^2$), fulfilling the resolution of unity

$$1 = \int_{\mathbb{S}^2} |\vartheta, \phi\rangle\langle\vartheta, \phi| \, d\Omega. \tag{35}$$

Coherent states are said to be "quasi-classical" because of their minimum uncertainty and area, and dynamical properties.

Using this coherent state (Bargmann) representation, we can associate a quasiprobability distribution (the so called Husimi function) to Hamiltonian eigenstates in the Landau $Q_L^{n,s}(\alpha) = \langle\alpha|\rho_L^{n,s}|\alpha\rangle$ and band $Q_B^{n,s}(\vartheta, \phi) = \langle\vartheta, \phi|\rho_B^{n,s}|\vartheta, \phi\rangle$ sectors respectively. Let us denote by

$$\mathcal{Q}_n(\alpha) = |\langle n|\alpha\rangle|^2 = \frac{e^{-|\alpha|^2}}{n!} |\alpha|^{2n} \tag{36}$$

the Husimi function of a Fock state $|n\rangle$ and by

$$\mathcal{Q}_c(\vartheta, \phi) = |\langle c|\vartheta, \phi\rangle|^2 = \cos^2(\vartheta/2), \quad \mathcal{Q}_v(\vartheta, \phi) = |\langle v|\vartheta, \phi\rangle|^2 = \sin^2(\vartheta/2), \tag{37}$$

the Husimi function of the conduction $|c\rangle = (1, 0)^t$ and valence $|v\rangle = (0, 1)^t$ band states, respectively. Note that $\mathcal{Q}_n$ only depends on $|\alpha|$ and $\mathcal{Q}_{c,v}$ only depend on ϑ. With this, the Husimi function of a Hamiltonian eigenstate can be written in

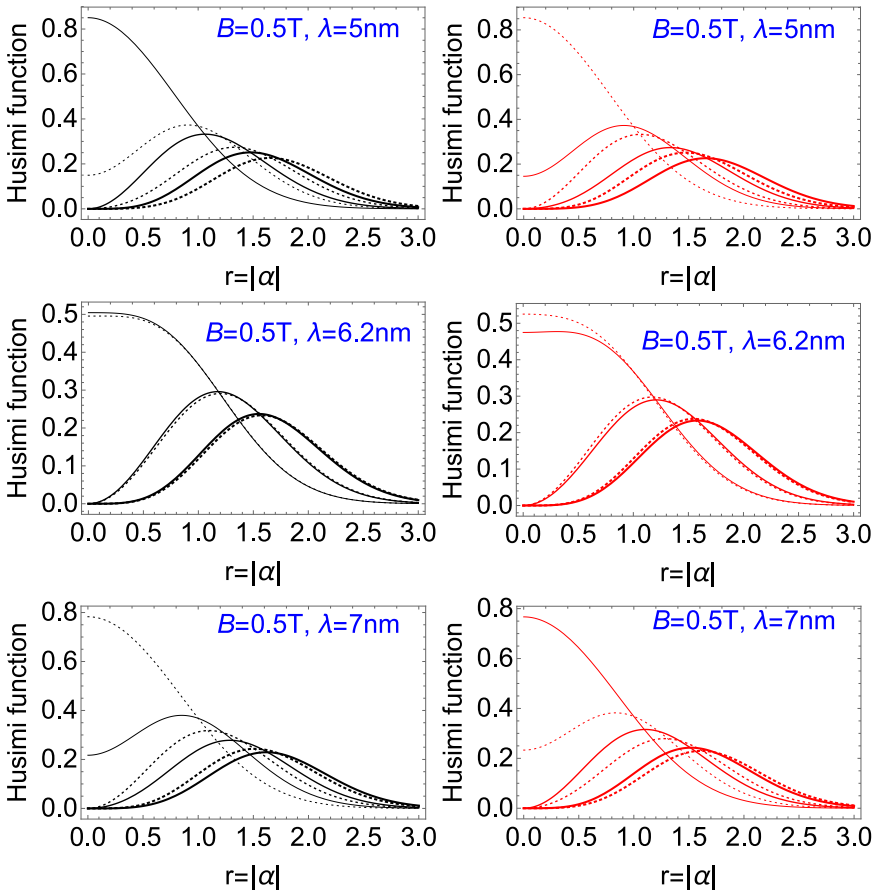

Fig. 8. Husimi function $Q_L^{n,s}(\alpha)$ (38) of the Hamiltonian eigenstates $|\boldsymbol{n}\rangle_s$, $n=\pm1,\pm2,\pm3$ (line thickness grows with $|n|$), in the Landau sector as a function of the radial coordinate $r=|\alpha|$. Solid/dotted (black/red) curves for electrons/holes (spin $s=\pm1$). The maximum of $Q_{\rho_L}(\alpha)$ decreases with $|n|$. From top to bottom, we go from the normal regime ($\lambda<\lambda_c$) to the inverted regime ($\lambda>\lambda_c$), crossing the critical pint $\lambda_c(B)=6.2$ nm for $B=0.5$ T.

the Landau sector as

$$Q_L^{n,s}(\alpha)=(A_n^s)^2\mathcal{Q}_{|n|-\frac{s+1}{2}}(\alpha)+(B_n^s)^2\mathcal{Q}_{|n|+\frac{s-1}{2}}(\alpha), \tag{38}$$

and in the band sector as

$$Q_B^{n,s}(\vartheta,\phi)=(A_n^s)^2\mathcal{Q}_c(\vartheta)+(B_n^s)^2\mathcal{Q}_v(\vartheta). \tag{39}$$

Note that, for Hamiltonian eigenvectors, $Q_L^{n,s}$ only depends on $r=|\alpha|$ and $Q_B^{n,s}$ only depends on ϑ. In Fig. 8 we represent the Husimi function $Q_L^{n,s}(\alpha)$ (38) of the Hamiltonian eigenstates $|\boldsymbol{n}\rangle_s$, $n=\pm1,\pm2,\pm3$, as a function of $r=|\alpha|$, before and after the critical point $\lambda_c(B)$. We see that the maximum of $Q_L^{n,s}(\alpha)$ decreases when $|n|$ increases, and it is located around $|\alpha|\simeq0$ for both $n=\pm1$ when $\lambda=\lambda_c(B)$. The roles of electrons and holes are reversed when crossing the critical point.

To quantify the spread/localization of a density matrix ρ in phase space, the ν-th moments of the corresponding Husimi function are often used. In our case, the ν-th moment of the Husimi function in the Landau sector with phase space $\mathbb{C}$ is

$$M_{n,s}^{\nu,L}=\int_{\mathbb{C}}\frac{d^2\alpha}{\pi}(Q_L^{n,s})^\nu(\alpha), \tag{40}$$

and the ν-th moment of the Husimi function in the band sector with phase space $\mathbb{S}^2$ is

$$M_{n,s}^{\nu,B}=\int_{\mathbb{S}^2}d\Omega\ (Q_B^{n,s})^\nu(\vartheta,\phi). \tag{41}$$

Note that, using (33),(35), we have $M_{n,s}^{1,L}=1=M_{n,s}^{1,B}$ as a consequence of the normalization of $\rho_{L,B}^{n,s}$. As we did in Section 3.4, we shall focus on the $\nu=2$ moment which, in this case, is related to the inverse area in phase space occupied by the

Husimi function. Before, we compute the auxiliary second moment of a Fock state

$$\mathcal{M}_n^2 \equiv \int_{\mathbb{C}} \frac{d^2\alpha}{\pi} \mathcal{Q}_n^2(\alpha) = \frac{(2n)!}{2^{2n+1}(n!)^2}, \tag{42}$$

which is maximum for $n = 0$, $M_0^2 = 1/2$. Likewise, we easily find

$$\mathcal{M}_{c,v}^2 \equiv \int_{\mathbb{S}^2} d\Omega\ \mathcal{Q}_{c,v}^2(\vartheta) = 2/3 \tag{43}$$

for the Husimi function second moments of conduction and valence band states (39). With this information, the Husimi function second moment of a Hamiltonian eigenstate in the Landau sector is

$$M_{n,s}^{2,L} = (A_n^s)^4 \mathcal{M}^2_{|n|-\frac{s+1}{2}} + (B_n^s)^4 \mathcal{M}^2_{|n|+\frac{s-1}{2}} + 2(A_n^s B_n^s)^2 \frac{(2|n|-1)!}{4^{|n|}|n|!(|n|-1)!}, \tag{44}$$

where we are using (42) and the value of $\int \frac{d^2\alpha}{\pi} \mathcal{Q}_{|n|}(\alpha)\mathcal{Q}_{|n|-1}(\alpha)$. Likewise, the Husimi function second moment of a Hamiltonian eigenstate in the band sector is

$$M_{n,s}^{2,B} = \frac{2}{3}(1 - (A_n^s B_n^s)^2), \tag{45}$$

where we are using (43), the value of $\int d\Omega\, \mathcal{Q}_c(\vartheta)\mathcal{Q}_v(\vartheta) = 1/3$ and the fact that $\rho_{L,B}^{n,s}$ is normalized.

Instead of $M_{n,s}^{2,L/B}$, we shall use the areas

$$A_L^{n,s} = 1/(2M_{n,s}^{2,L}),\ A_B^{n,s} = 2/(3M_{n,s}^{2,B}), \tag{46}$$

occupied by $\rho_L^{n,s}$ and $\rho_B^{n,s}$ in phase spaces $\mathbb{C}$ and $\mathbb{S}^2$, respectively, which have been properly normalized so that the minimum area in both cases is $A = 1$. Indeed, as conjectured by Wehrl [58], proved by Lieb [59] and extended to more general phase spaces in [60–63], the normalized area A_ρ of a density matrix ρ in phase space verifies $A_\rho \geq 1$, attaining its minimum value when ρ corresponds to a coherent state. Actually, these theorems are not stated in terms of area in phase space but in terms of the so called Rényi–Wehrl entropy $W_\rho^\nu = \frac{1}{1-\nu}\ln(M_\rho^\nu)$ (M_ρ^ν denotes the ν-th moment of ρ) and, in particular, in terms of the Wehrl entropy

$$W_\rho = \lim_{\nu\to 1} W_\rho^\nu = -\int_{\mathbb{P}} Q_\rho(z) \ln\left(Q_\rho(z)\right) d\mu(z) \tag{47}$$

for the Husimi function Q_ρ of ρ in phase space $\mathbb{P} \ni z$ with integration measure $d\mu(z)$. Both, area and Wehrl entropy, are minimal in the case that ρ corresponds to a coherent state. Therefore, they measure the delocalization of a state ρ in phase space.

In Fig. 9 we represent the area occupied in phase spaces $\mathbb{C}$ and $\mathbb{S}^2$ (Landau and band sectors), respectively, by the Hamiltonian eigenstates $|\boldsymbol{n}\rangle_s$ for low-lying Landau levels $n = \pm 1, \pm 2, \pm 3$, as a function of the HgTe layer thickness λ. In the Landau sector, lower Landau levels occupy an area smaller (are more coherent) than higher Landau levels. As can be seen in Fig. 9 (top left panel), conduction and valence states suffer an area inversion at the HTPT critical point $\lambda_c^{n,s}$ (the same behavior for spin up and down). Moreover, the total area of electrons ($n > 0$) plus holes ($n < 0$) displays a maximum at $\lambda_c^{n,s}$ (bottom left panel of Fig. 9), just as the total area of spin up plus spin down electrons/holes (bottom right panel of Fig. 9). In the band sector, the behavior is simpler (top right panel of Fig. 9) since conduction and valence states occupy the same area. Higher energy Hamiltonian eigenstates occupy a higher area in phase space $\mathbb{S}^2$, and the maximum delocalization for all of them occurs at the HTPT critical point $\lambda_c^{n,s}(B)$. In fact, as we have already noted before for other information measures, the corresponding maxima are slightly displaced to the right with respect to the TPT critical point $\lambda_c(B) = 6.2$ nm for $B = 0.5$ T, according to the values of $\lambda_c^{n,s}(0.5)$ in Table 2.

4. Conclusions

Using different information measures like purity, quantum fluctuations, fidelity susceptibility and other generalized entropies, we have found that higher Landau levels $|\boldsymbol{n}(\lambda)\rangle_s$, $|n| > 0$, of HgTe quantum wells suffer an "electron–hole" transition at a critical value $\lambda_c^{n,s}(B)$ of the HgTe layer thickness λ for a given applied magnetic field B. The localization of the critical point occurs when the system has the same probability to be in the valence and conduction bands. The critical points $\lambda_c^{n,s}(B)$ appear to be slightly shifted (for low $|n|$ and B) with respect to standard TPT critical point $\lambda_c(B)$ (obtained from edge state $n = 0$ band inversion) separating the normal (quantum Hall) from the inverted (spin quantum Hall) regimes. Therefore, from this point of view, higher Landau level transition points $\lambda_c^{n,s}(B)$ could be considered as "echoes" of the ordinary topological phase transition (TPT) occurring at $\lambda_c(B)$. This fact leads us to introduce the concept of "higher Landau level topological phase transition" (HTPT for short) of which information measures account for and provide sharp signatures. In summary, information measurements and markers provide a useful tool to visualize and understand topological phase transitions, complementary to conventional topological numbers, allowing an extension from edge and ground states to higher Landau levels. Furthermore, these information measurements show that, at critical points, the wave function is delocalized and there is a growth of entanglement and quantum fluctuation of some observables, showing a relationship between quantum information and quantum phases of matter and giving a different point of view to understand topological phase transitions.

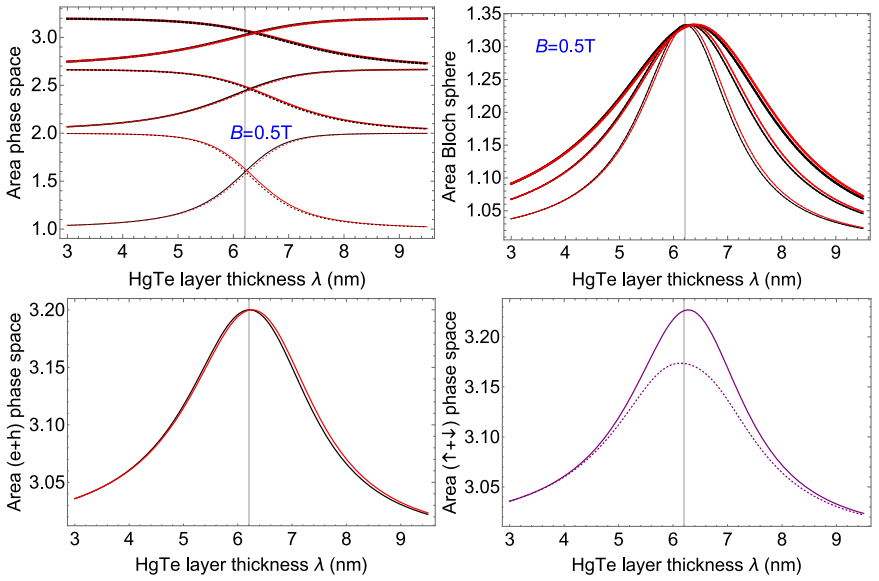

Fig. 9. Top panel: Area in phase space $\mathbb{C}$ (Landau sector, left panel) and area in the Bloch sphere $\mathbb{S}^2$ (band sector, right panel) for electrons $n > 0$ (solid lines) and holes $n < 0$ (dotted lines) of Hamiltonian eigenstates $|\boldsymbol{n}(\lambda)\rangle_s$ of a HgTe/CdTe quantum well for a magnetic field of $B = 0.5$ T as a function of the HgTe layer thickness λ for Landau levels $n = \pm 1, \pm 2, \pm 3$ (line thickness grows with $|n|$), black lines for spin $s = 1$ and red lines for $s = -1$. The vertical gray grid line indicates the critical HgTe thickness $\lambda_c(0.5) \simeq 6.2$ nm separating normal (QH) from inverted (QSH) regimes. Bottom panel: combined electron plus hole (left panel) and spin up plus down (right panel) areas in phase space $\mathbb{C}$ (Landau sector) for $|n| = 1$.

CRediT authorship contribution statement

Manuel Calixto: Writing – original draft, Conceptualization, Methodology, Software, Formal analysis, Investigation, Resources, Visualization, Funding acquisition. **Nicolás A. Cordero:** Visualization, Investigation, Resources, Writing – review & editing. **Elvira Romera:** Conceptualization, Methodology, Writing – review & editing. **Octavio Castaños:** Conceptualization, Methodology, Software, Investigation, Writing – review & editing, Supervision.

Declaration of competing interest

The authors declare that they have no known competing financial interests or personal relationships that could have appeared to influence the work reported in this paper.

Data availability

Data will be made available on request.

Acknowledgments

We thank the support of the Spanish MICINN through the project PGC2018-097831-B-I00 and Junta de Andalucía, Spain through the projects UHU-1262561 and FQM-381. Funding for open access charge: Universidad de Granada / CBUA.

References

[1] Tian-Yi Zhang, Qing Yan, Qing-Feng Sun, Constructing low-dimensional quantum devices based on the surface state of topological insulators, Chin. Phys. Lett. 38 (7) (2021) 077303.
[2] Michelle J.S. Spencer, Tetsuya Morishita (Eds.), Silicene: Structure, Properties and Applications, in: Springer Series in Materials Science, vol. 235, 2016.
[3] L. Stille, C.J. Tabert, E.J. Nicol, Optical signatures of the tunable band gap and valley-spin coupling in silicene, Phys. Rev. B 86 (2012) 195405.
[4] C.J. Tabert, E.J. Nicol, Valley-spin polarization in the magneto-optical response of silicene and other similar 2D crystals, Phys. Rev. Lett. 110 (2013) 197402.
[5] C.J. Tabert, E.J. Nicol, Magneto-optical conductivity of silicene and other buckled honeycomb lattices, Phys. Rev. B 88 (2013) 085434.
[6] M. Tahir, U. Schwingenschlögl, Valley polarized quantum Hall effect and topological insulator phase transitions in silicene, Sci. Rep. 3 (1) (2013) 1075.
[7] Shun-Qing Shen, Topological Insulators: Dirac Equation in Condensed Matters, Springer-Verlag Berlin Heidelberg, 2012.
[8] B. Andrei Bernevig, Topological Insulators and Topological Superconductors, Princeton University Press, 2013.

[9] L. Oroszlany J.K. Asboth, A. Palyi, A. Short, A Short Course on Topological Insulators: Band Structure and Edge States in One and Two Dimensions, Springer International Publishing Switzerland, 2016.
[10] M.Z. Hasan, C.L. Kane, Colloquium: Topological insulators, Rev. Modern Phys. 82 (2010) 3045–3067.
[11] Xiao-Liang Qi, Shou-Cheng Zhang, Topological insulators and superconductors, Rev. Modern Phys. 83 (2011) 1057–1110.
[12] Liangzhi Kou, Yandong Ma, Ziqi Sun, Thomas Heine, Changfeng Chen, Two-dimensional topological insulators: Progress and prospects, J. Phys. Chem. Lett. 8 (8) (2017) 1905–1919.
[13] C.L. Kane, E.J. Mele, Quantum Spin Hall effect in graphene, Phys. Rev. Lett. 95 (2005) 226801.
[14] B. Andrei Bernevig, Taylor L. Hughes, Shou-Cheng Zhang, Quantum spin hall effect and topological phase transition in HgTe quantum wells, Science 314 (5806) (2006) 1757–1761, arXiv:https://www.science.org/doi/pdf/10.1126/science.1133734.
[15] Markus König, Steffen Wiedmann, Christoph Brüne, Andreas Roth, Hartmut Buhmann, Laurens W. Molenkamp, Xiao-Liang Qi, Shou-Cheng Zhang, Quantum spin hall insulator state in HgTe quantum wells, Science 318 (5851) (2007) 766–770, arXiv:https://www.science.org/doi/pdf/10.1126/science.1148047.
[16] O Castaños, R López-Peña, E Nahmad-Achar, J.G. Hirsch, Quantum information approach to the description of quantum phase transitions, J. Phys. Conf. Ser. 403 (2012) 012003.
[17] E. Romera, M. Calixto, A. Nagy, Entropic uncertainty and the quantum phase transition in the Dicke model, Europhys. Lett. 97 (2) (2012) 20011.
[18] Octavio Castaños, Manuel Calixto, Francisco Pérez-Bernal, Elvira Romera, Identifying the order of a quantum phase transition by means of Wehrl entropy in phase space, Phys. Rev. E 92 (2015) 052106.
[19] Á. Nagy, M. Calixto, E. Romera, A density functional theory view of quantum phase transitions, J. Chem. Theory Comput. 9 (2) (2013) 1068–1072, http://dx.doi.org/10.1021/ct301015n, PMID: 26588749.
[20] M. Calixto, R. del Real, E. Romera, Husimi distribution and phase-space analysis of a vibron-model quantum phase transition, Phys. Rev. A 86 (2012) 032508.
[21] Hong-Chen Jiang, Zhenghan Wang, Leon Balents, Identifying topological order by entanglement entropy, Nat. Phys. 8 (12) (2012) 902–905.
[22] Bei Zeng, Xie Chen, Duan-Lu Zhou, Xiao-Gang Wen, Quantum Information Meets Quantum Matter: From Quantum Entanglement to Topological Phases of Many-Body Systems, Springer Nature, 2019.
[23] M. Calixto, E. Romera, Identifying topological-band insulator transitions in silicene and other 2D gapped Dirac materials by means of Rényi-Wehrl entropy, EPL (Europhys. Lett.) 109 (4) (2015) 40003.
[24] E. Romera, M. Calixto, Uncertainty relations and topological-band insulator transitions in 2D gapped Dirac materials, J. Phys.: Condens. Matter 27 (17) (2015) 175003.
[25] M. Calixto, E. Romera, Inverse participation ratio and localization in topological insulator phase transitions, J. Stat. Mech. Theory Exp. 2015 (6) (2015) P06029.
[26] E. Romera, M. Calixto, Band inversion at critical magnetic fields in a silicene quantum dot, EPL (Europhys. Lett.) 111 (3) (2015) 37006.
[27] E. Romera, M. Calixto, J.C. Bolívar, Information measures and topological-band insulator transitions in 2D-Dirac materials under external circularly polarized lasers, and static electric and magnetic fields, Physica A 511 (2018) 174–181.
[28] Octavio Castaños, Elvira Romera, Manuel Calixto, Information theoretic analysis of Landau levels in monolayer phosphorene under magnetic and electric fields, Mater. Res. Express 6 (10) (2019) 106316.
[29] Manuel Calixto, Elvira Romera, Octavio Castaños, Analogies between the topological insulator phase of 2D Dirac materials and the superradiant phase of atom-field systems, Int. J. Quantum Chem. 121 (4) (2021) e26464, arXiv:https://onlinelibrary.wiley.com/doi/pdf/10.1002/qua.26464.
[30] Charles L. Kane, Eugene J. Mele, A new spin on the insulating state, Science 314 (5806) (2006) 1692–1693, arXiv:https://www.science.org/doi/pdf/10.1126/science.1136573.
[31] E.G. Novik, A. Pfeuffer-Jeschke, T. Jungwirth, V. Latussek, C.R. Becker, G. Landwehr, H. Buhmann, L.W. Molenkamp, Band structure of semimagnetic $Hg_{1-y}Mn_yTe$ quantum wells, Phys. Rev. B 72 (2005) 035321.
[32] Markus König, Hartmut Buhmann, Laurens W. Molenkamp, Taylor Hughes, Chao-Xing Liu, Xiao-Liang Qi, Shou-Cheng Zhang, The quantum Spin Hall effect: Theory and experiment, J. Phys. Soc. Japan 77 (3) (2008) 031007, http://dx.doi.org/10.1143/JPSJ.77.031007.
[33] Yan-Feng Zhou, Hua Jiang, X.C. Xie, Qing-Feng Sun, Two-dimensional lattice model for the surface states of topological insulators, Phys. Rev. B 95 (2017) 245137.
[34] Sebastian Diehl, Enrique Rico, Mikhail A. Baranov, Peter Zoller, Topology by dissipation in atomic quantum wires, Nat. Phys. 7 (12) (2011) 971–977.
[35] C.-E. Bardyn, M.A. Baranov, C.V. Kraus, E Rico, A İmamoğlu, P Zoller, S Diehl, Topology by dissipation, New J. Phys. 15 (8) (2013) 085001.
[36] Jan Carl Budich, Peter Zoller, Sebastian Diehl, Dissipative preparation of chern insulators, Phys. Rev. A 91 (2015) 042117.
[37] V.M. Martinez Alvarez, J.E. Barrios Vargas, M. Berdakin, L.E.F. Foa Torres, Topological states of non-Hermitian systems, Eur. Phys. J. Spec. Top. 227 (12) (2018) 1295–1308.
[38] Luis E.F. Foa Torres, Perspective on topological states of non-Hermitian lattices, J. Phys.: Mater. 3 (1) (2019) 014002.
[39] Fei Song, Shunyu Yao, Zhong Wang, Non-Hermitian Skin effect and chiral damping in open quantum systems, Phys. Rev. Lett. 123 (2019) 170401.
[40] Dan S. Borgnia, Alex Jura Kruchkov, Robert-Jan Slager, Non-Hermitian boundary modes and topology, Phys. Rev. Lett. 124 (2020) 056802.
[41] Huitao Shen, Bo Zhen, Liang Fu, Topological band theory for non-Hermitian Hamiltonians, Phys. Rev. Lett. 120 (2018) 146402.
[42] M. Belén Farias, Solofo Groenendijk, Thomas L. Schmidt, Generalized Chern numbers based on open system Green's functions, New J. Phys. 23 (7) (2021) 073009.
[43] N.D. Drummond, V. Zólyomi, V.I. Fal'ko, Electrically tunable band gap in silicene, Phys. Rev. B 85 (2012) 075423.
[44] Cheng-Cheng Liu, Wanxiang Feng, Yugui Yao, Quantum Spin Hall effect in silicene and two-dimensional germanium, Phys. Rev. Lett. 107 (2011) 076802.
[45] Cheng-Cheng Liu, Hua Jiang, Yugui Yao, Low-energy effective Hamiltonian involving spin-orbit coupling in silicene and two-dimensional germanium and tin, Phys. Rev. B 84 (2011) 195430.
[46] Wei-Feng Tsai, Cheng-Yi Huang, Tay-Rong Chang, Hsin Lin, Horng-Tay Jeng, A. Bansil, Gated silicene as a tunable source of nearly 100% spin-polarized electrons, Nature Commun. 4 (1) (2013) 1500.
[47] B. Büttner, C.X. Liu, G. Tkachov, E.G. Novik, C. Brüne, H. Buhmann, E.M. Hankiewicz, P. Recher, B. Trauzettel, S.C. Zhang, L.W. Molenkamp, Single valley Dirac fermions in zero-gap HgTe quantum wells, Nat. Phys. 7 (5) (2011) 418–422.
[48] Benedikt Scharf, Alex Matos-Abiague, Jaroslav Fabian, Magnetic properties of HgTe quantum wells, Phys. Rev. B 86 (2012) 075418.
[49] Benedikt Scharf, Alex Matos-Abiague, Igor Žutić, Jaroslav Fabian, Probing topological transitions in HgTe/Cdte quantum wells by magneto-optical measurements, Phys. Rev. B 91 (2015) 235433.
[50] M.A. Caprio, P. Cejnar, F. Iachello, Excited state quantum phase transitions in many-body systems, Ann. Physics 323 (5) (2008) 1106–1135.
[51] P. Pérez-Fernández, A. Relaño, J.M. Arias, P. Cejnar, J. Dukelsky, J.E. García-Ramos, Excited-state phase transition and onset of chaos in quantum optical models, Phys. Rev. E 83 (2011) 046208.
[52] Paolo Zanardi, Nikola Paunković, Ground state overlap and quantum phase transitions, Phys. Rev. E 74 (2006) 031123.

[53] Wen-Long You, Ying-Wai Li, Shi-Jian Gu, Fidelity, dynamic structure factor, and susceptibility in critical phenomena, Phys. Rev. E 76 (2007) 022101.
[54] Shi-Jian Gu, Fidelity approach to quantum phase transitions, Internat. J. Modern Phys. B 24 (23) (2010) 4371–4458, http://dx.doi.org/10.1142/S0217979210056335.
[55] Sergio Cordero, Eduardo Nahmad-Achar, Ramón López-Peña, Octavio Castaños, Quantum phase diagrams of matter-field Hamiltonians I: Fidelity, bures distance, and entanglement, Phys. Scr. 96 (3) (2021) 035104.
[56] R López-Peña, S Cordero, E Nahmad-Achar, O Castaños, Quantum phase diagrams of matter-field Hamiltonians II: Wigner function analysis, Phys. Scr. 96 (3) (2021) 035103.
[57] J.M. Radcliffe, Some properties of coherent spin states, J. Phys. A: Gen. Phys. 4 (3) (1971) 313–323.
[58] Alfred Wehrl, General properties of entropy, Rev. Modern Phys. 50 (1978) 221–260.
[59] Elliott H. Lieb, Proof of an entropy conjecture of Wehrl, Comm. Math. Phys. 62 (1) (1978) 35–41.
[60] Sven Gnutzmann, Karol Zyczkowski, Rényi-Wehrl entropies as measures of localization in phase space, J. Phys. A: Math. Gen. 34 (47) (2001) 10123–10139.
[61] Ayumu Sugita, Proof of the generalized Lieb-Wehrl conjecture for integer indices larger than one, J. Phys. A: Math. Gen. 35 (42) (2002) L621–L626.
[62] Florian Mintert, Karol Życzkowski, Wehrl entropy, Lieb conjecture, and entanglement monotones, Phys. Rev. A 69 (2004) 022317.
[63] Elliott H. Lieb, Jan Philip Solovej, Proof of the Wehrl-type entropy conjecture for symmetric SU(N) coherent states, Comm. Math. Phys. 348 (2) (2016) 567–578.